
Reaction Dynamics and Charge Transfer in the Scattering of State-Selected Ions on Surfaces

Patricia L. Maazouz

Publication Date

15-04-2004

License

This work is made available under a All Rights Reserved license and should only be used in accordance with that license.

Citation for this work (American Psychological Association 7th edition)

Maazouz, P. L. (2004). *Reaction Dynamics and Charge Transfer in the Scattering of State-Selected Ions on Surfaces* (Version 1). University of Notre Dame. <https://doi.org/10.7274/7h149p30z5r>

This work was downloaded from CurateND, the University of Notre Dame's institutional repository.

For more information about this work, to report or an issue, or to preserve and share your original work, please contact the CurateND team for assistance at curate@nd.edu.

CHAPTER 2

EXPERIMENTAL APPARATUS AND PROCEDURES

2.1. Introduction

In order to accurately assess the interactions between gas projectiles and well-characterized surfaces, the unwanted gas molecules from ambient air must be removed from the environment. Therefore, experiments are performed in the ultrahigh vacuum (UHV) chamber shown in Figure 2.1.^{1,2} Prior to the scattering experiments, the surface is cleaned with an ion-sputtering gun and through annealing cycles, surface order and cleanliness are characterized via Low Energy Electron Diffraction (LEED) and Auger electron spectroscopy (AES) within the main chamber. The incident state-selected ions are formed via resonance enhanced multiphoton ionization (REMPI) at the intersection of a pulsed molecular beam and a pulsed ultraviolet laser within the UHV scattering chamber. The resulting ions are accelerated by electrostatic lenses, mass-selected within a Wien filter, and decelerated to the final beam energy (5-105 eV). The packets of state-selected ions are directed to a clean crystal surface at normal incidence.

The incident and scattered ions are monitored with a novel ion-imaging detector, specifically designed to afford mass-, angle-, and velocity-resolution with near single-ion detection efficiency.⁴⁻⁶ The spatial distribution of ions is recorded on a CCD camera at a particular instant in time. The digitized image reflects the ions' two-dimensional

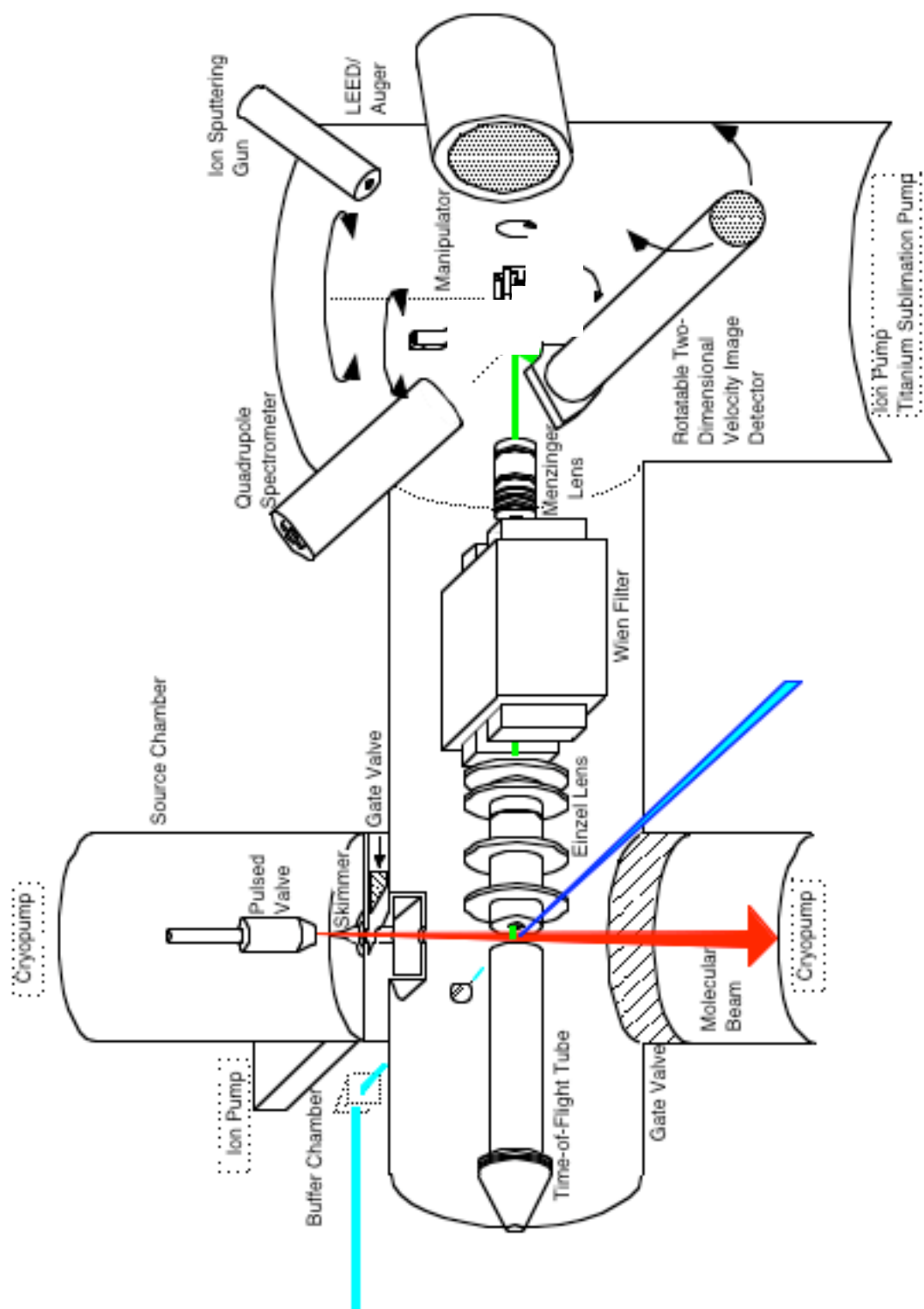


Figure 2.1. Schematic diagram of the experimental apparatus. (Reproduced with permission from Ref.1).

velocity distribution in the scattering plane. The imaging detector is positioned along the ion-beam axis, collinear with the surface normal. The solid angle over which ions are collected is $\pm 28^\circ$ (in-plane) and $\pm 7^\circ$ (out-of-plane) relative to the surface normal. This normal-incidence/normal-detection scattering geometry enables the detector to collect incident Br^+ ions and scattered ionic products on alternating laser shots. In this way, a relative ion yield is calculated from the number of collected product ions, integrated over all velocities within the acceptance angle of the detector, divided by the number of incident ions.

The remainder of this chapter focuses on describing the chamber design, preparation of the surface, state-selected ions transport to the surface, and detection of the incident and scattered ions. The last section describes how the detection efficiency, TOF distribution, and mass resolution of the scattered ions were optimized.

2.2 Chamber Design

The UHV chamber utilized in the current scattering experiments is divided into two main sections—the source chamber and the main scattering–surface preparation chamber. In order to accommodate high gas load in the source chamber and a UHV environment in the main chamber, a three-stage pumping scheme is utilized. A chemically resistant Leybold Trivac D40-BCS rotary vane vacuum pump is utilized to pump highly reactive gases from the source chamber down to 10^{-3} Torr. After this vacuum is achieved, the rotary vane pump is isolated from the pumping lines and a Leybold RPK 900 cryogenic pump maintains the base source pressure below 10^{-6} Torr. An additional Leybold cryopump and a Perkin-Elmer ion pump /Ti sublimation pump system keep the pressure below 10^{-9} Torr in the main chamber.

Prior to any experiments, contaminants, especially water, are removed from the main chamber during a weeklong bake-out. Heaters, located at various sites on the exterior of the chamber, are turned on for uniform heating of the stainless steel chamber. The temperatures at various sites on the chamber are monitored throughout the bake-out to ensure that the temperatures are not damaging to sensitive equipment and that the chamber is warm enough to remove the contamination. A quadrupole mass spectrometer (QMS) is utilized to monitor the quantities of H₂, H₂O and CO—the major contaminants in the chamber. When the main chamber pressure sustains a minimum value near 10⁻⁸ Torr during the bake-out, the heaters are turned off, and the main chamber pressure stabilizes to pressures below 4x10⁻¹⁰ Torr.

2.3 Surface Preparation

The ability to accurately and thoroughly describe the reaction dynamics for a scattering system requires the use of a clean and well-characterized surface. In order to clean the metal surface and to elevate the surface temperature during scattering experiments, the crystal mount contains connections for heater wires and thermocouple wires. In addition, the crystal face is mounted perpendicular to the path of the ion packets to ensure that the normal incidence/normal scattering geometry is achieved. The cleaning procedure for each crystal surface is well documented in the literature, and typically involves numerous cycles of ion sputtering and surface annealing. For sputtering, an ion gun is employed to direct energetic inert gas ions at glancing angles to the surface to “knock-off” undesirable atoms or molecules from the surface without implanting into the bulk of the crystal. An electrical current is applied to tungsten wires surrounding the crystal surface to heat the metal to temperatures that cause contaminants to desorb from the surface. The cleanliness of the surface is monitored by AES and the

surface structure is verified by recording LEED images that can be directly compared to images reported in the literature.

The incident ions arrive at the surface in well-defined ion packets, rather than a continuous ion beam. Consequently, for scattering experiments performed at elevated temperatures, pulsed currents are applied to the resistive heater wires during the time interval when the ions are far from the surface. Since the incident and scattered projectiles are charged particles, the pulsing scheme is necessary to prevent stray electric and magnetic fields from modifying the path of the ions. Figure 2.2 shows the electronic circuit diagram utilized for the pulsed voltages and the synchronization relative to the time at which the laser fires. The 200 μ s width of the blank pulse is chosen such that at any collision energy, both incident and scattered ions experience a field-free region near the surface. When a TTL pulse (5 V) from the delay generator reaches the fast-switching power field effect transistor (FET) RFK45N05, the circuit closes allowing a 4.5 amp current to resistively heat the surface to temperatures up to 400°C. When the ions are in the near-surface region, a low voltage output (<0.1 V) from the delay generator opens the circuit preventing any resistive heating of the surface. In order to maintain a constant T_s , the resistive heating circuit is closed for the maximum time possible, and T_s is closely monitored throughout the scattering experiments to ensure that the pulsing scheme does not create significant fluctuations. For T_s above 400°C, the heater wires begin to glow, producing background light that compromises the images of scattered ions. Overall, the actual T_s did not fluctuate more than $\pm 2.5\%$ from the desired elevated value for the duration of each scattering experiment.

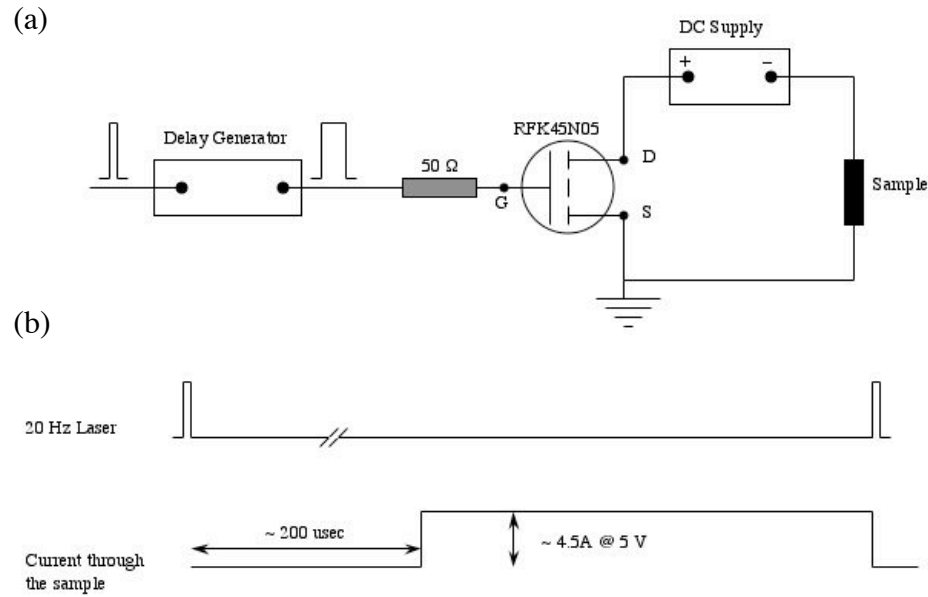


Figure 2.2 (a) Electronic schematic utilized to create a pulsed DC voltage on the surface to resistively heat the surface. The trigger pulse from the laser initiates a 200 μ s blanking pulse at the field effect transistor (FET) RFK45N05. (b) Synchronization of laser and sample heating pulsess. $\sim 200 \mu$ s after the Nd:YAG laser is fired, the FET closes until the next laser pulse allowing a current ~ 4.5 A at 5 V DC to flow through the sample.

2.4 Ion Beam Source and Transport

The ability to determine the affect of incident vibrational energy on the reaction dynamics requires an experimental method to produce state-selected ions. Therefore, REMPI is utilized to prepare incident ions in a particular rovibrational state. Since the current apparatus is not equipped with experimental techniques (e.g., photoelectron spectroscopy) to determine the vibrational purity of the state-selected species, the selection of incident projectiles is limited to molecules, such as NO^+ , NH_3^+ , and Br_2^+ ,⁷ whose state purity has been established in prior experiments. The REMPI processes for the molecules utilized in the current studies produce state-selected ions with vibrational purities greater than 79%.^{2,8}

Although several REMPI schemes are available to produce incident projectiles in a specific rovibrational state, both Br_2^+ and NO^+ utilize the (2+1) REMPI scheme as illustrated in Fig. 2.3. This process involves the excitation of ground-state neutral molecules to the Rydberg state by the absorption of two photons followed by a subsequent excitation to the desired rovibrational level of the ground ionic electronic state by the absorption of one additional photon. A strong propensity for rovibrational selectivity of the ion occurs if the Rydberg state belongs to a series that converges on the ground state of the ion. Not only does this method of ionization offer exceptional selectivity, but REMPI also provides a high degree of state purity because the ion optics will only extract those molecules that have undergone the REMPI process.

State-selected molecular ions are created at the intersection of a pulsed molecular beam and a focused pulsed laser. A 20-Hz frequency-doubled Nd:YAG (Continuum)-pumped dye laser (Continuum) provides 6 ns tunable ultraviolet light pulses for REMPI. The tunable dye laser allows for the selection of a particular wavelength corresponding to the creation of incident ions in a specific rovibrational state. The neutral gas molecules are supersonically expanded through a pulsed nozzle (General

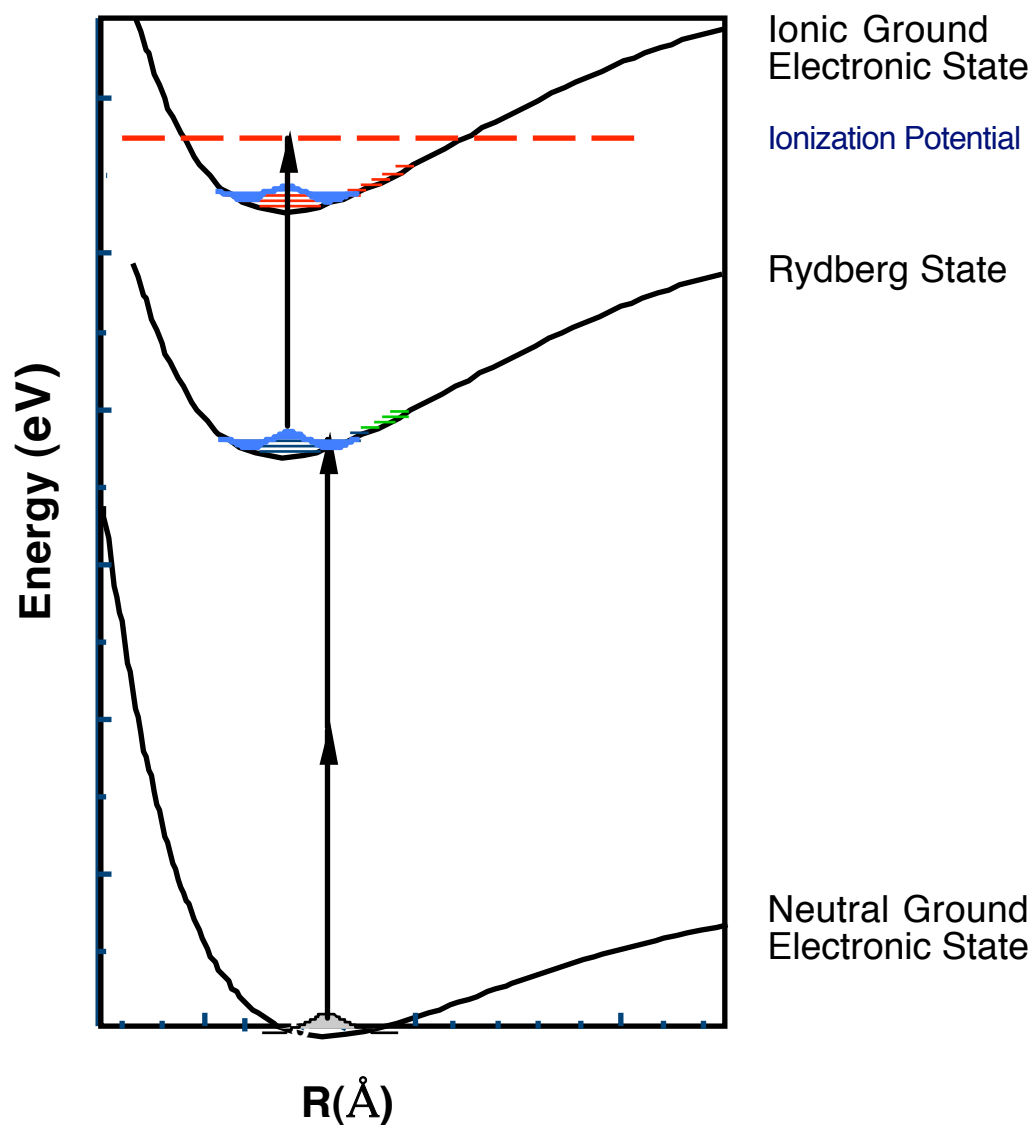


Figure 2.3 Generic (2+1) REMPI scheme for producing state-selected incident molecular ions. The neutral molecules absorb two photons with a specific amount of energy to become excited to the Rydberg electronic state. The absorption of one additional photon excites the molecule from the Rydberg state to the ground electronic state of the ion with the same rovibrational character as the Rydberg state.

Valve) with a 150 mm orifice. The number of incident ions created in each ion packet is controlled by the backing pressure behind the nozzle and the intensity of the output from the dye laser. A typical ion packet delivers approximately 10^3 ions to the surface every laser pulse.

The ions can be extracted towards the time-of-flight tube to optimize the REMPI process or towards the surface for scattering. When the ions are extracted in the former case, the intensity of nascent ions is measured as a function of the dye laser wavelength and compared to spectra reported in the literature. The laser wavelength is parked on a transition to populate the desired rovibrational state. When the ions are extracted towards the surface, they are accelerated to 200 eV, mass-selected in the Wien filter, and finally decelerated to a final beam energy between 5 and 105 eV. The selection of the final beam energy and the intensity of the ion packets are optimized by adjusting the voltages applied to each optic along the transport system via a novel Labview[®] Ion Optics program. For each incident projectile the ion optic settings are optimized and saved corresponding to a series of desired final beam energies that can be subsequently accessed during the scattering experiments.

Calibrating the ion beam collision energy is the final step in the preparation of the incident ion packets. The manipulator is adjusted along the z -axis to align a repeller plate, located below the surface mount, perpendicular to the axis of the incident ion beam. A positive potential within 10 volts of the expected ion packet final energy is applied to the repeller plate. As the incident ions emerge from the final deceleration lens, they either reflect away from the repeller if the bias voltage is larger than the ion energy or they collide with the repeller if the bias voltage is too low. The intensity of reflected ions is measured with the ion-imaging detector (Section 2.5) as a function of the repeller voltage. The final beam energy is calibrated to the repeller voltage at which the reflected ions reach half the maximum intensity.

2.5 Ion Detection

2.5.1 Operation

Both incident and scattered ions are monitored using an ion imaging detector (flyswatter) with near single-ion collection efficiency.⁴⁻⁶ The detector is mounted on an 8" O.D. rotatable platform (Thermionics). Figure 2.4 illustrates the configuration of the flyswatter relative to the final ion transport optics and the surface. In the most common configuration, both the incident ion beam and the detector lie along the surface normal. In addition, an azimuthal rotation of the surface sample allows for product ion collection within any crystallographic scattering plane. Figure 2.5a provides a cross-sectional view detailing the current arrangement of elements in the flyswatter detector. The flyswatter consists of a pulsed repeller plate that runs parallel to a permanently grounded grid. The incident ions pass between the grounded repeller and the grid before colliding with the surface, and the product ions traverse through this region after scattering from the surface. At a predetermined swat delay relative to the laser trigger, a ~ 1000 V pulse, of equal polarity as the ions to be detected, is placed on the repeller plate, and a ~ 1000 V pulse, of opposite polarity, is placed on the flight tube. This action accelerates the ions in a direction normal to the plates while preserving their spatial distribution. The ions drift through a field-free flight tube before being accelerated into a pair of pulsed channel electron multiplier array (CEMA) plates. Each ion that impacts the 40 mm diameter, image-quality CEMA plates (Galileo) produces $\sim 10^7$ secondary electrons. These electrons accelerate towards a phosphor screen (Kimball Physics), biased at +4 kV relative to the rear CEMA plate, producing a burst of light ($< 300 \mu\text{m}$ diameter) that is captured by a charged coupled device (CCD) camera. The images are sent to a frame grabber board located inside a Macintosh G3 computer, where they are digitized, processed, and stored for analysis.

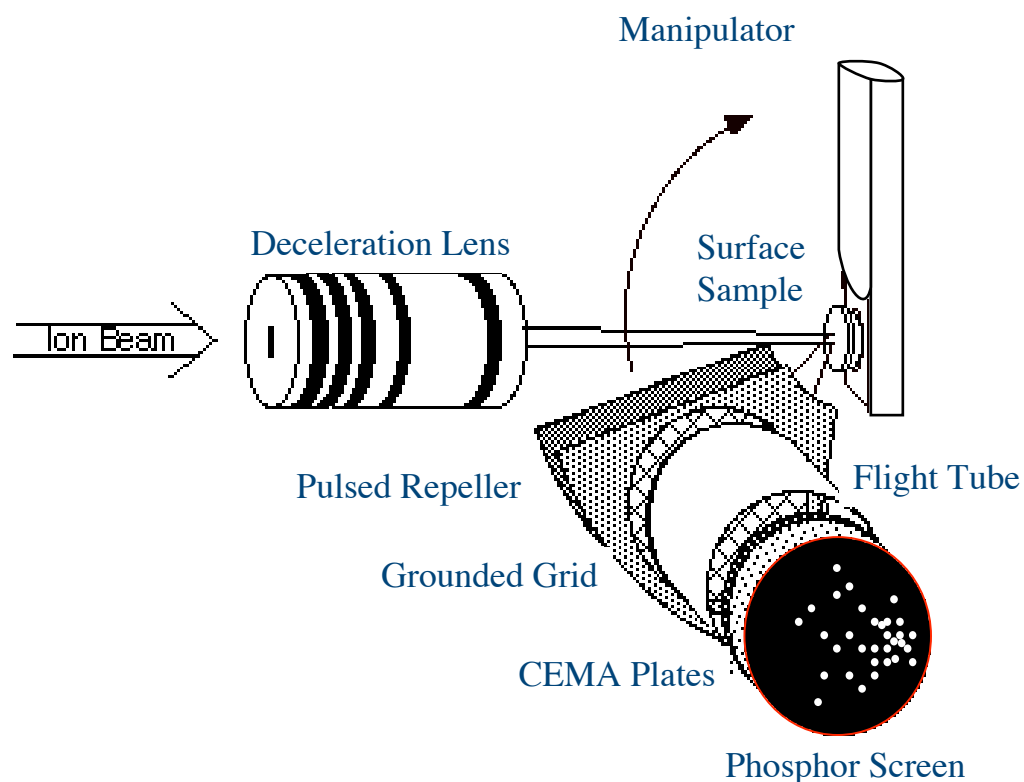


Figure 2.4 A schematic of the ion imaging detector (flyswatter). The ion beam exits the Menzinger deceleration lens and is directed toward the surface sample manipulator. Although the detector is rotatable, the center of the phosphor screen is aligned with the center of the ion beam axis in the current experiments. (Reproduced with permission from Ref. 6).

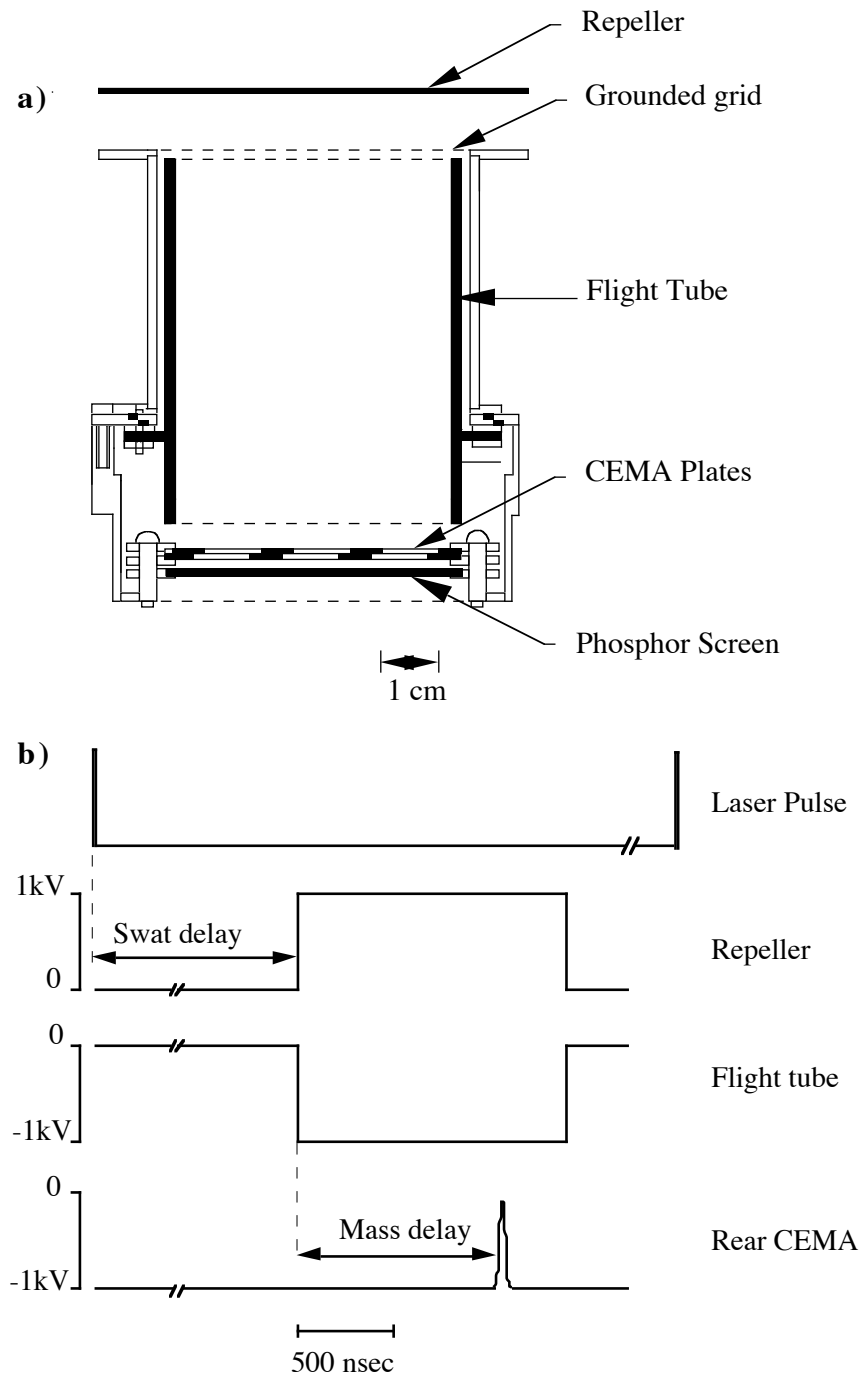


Figure 2.5 a) An assembly drawing of the flyswatter detector. b) Sequence of voltage pulses applied to the flyswatter optics. (Reproduced with permission from Ref. 4).

Ions of different mass will experience different flight times through the detector. Lighter ions will have a larger velocity than heavier ions upon acceleration into the flight tube; hence, lighter ions will arrive at the CEMA plates earlier in time. The flyswatter exploits this idea to achieve mass-resolution. Wiley and McLaren developed a set of focusing conditions to compensate for the distribution of initial ion positions between the repeller and the grid when the swat pulse fires.⁹ More advanced optimizations can reduce the broadening associated with the dispersion of initial ion velocities along the direction normal to the repeller.¹⁰ By gating the CEMA plates, ions of only one particular mass are allowed to contribute to the resulting image. The pair of CEMA plates is simmered at 1100 VDC. At a preset mass delay relative to the swat pulse on the repeller, an additional 900 V pulse (Directed Energy, Inc.) of 25 ns duration is applied to the rear CEMA plate. During the mass pulse, the CEMA plates are biased with a total of 2000 V, and virtually every ion that impacts the CEMA plates produces a spatially localized electron cascade event. In contrast, ions that strike the CEMA plates before or after the mass pulse are amplified with negligible gain, because the CEMA plates have only an 1100 V bias. Consequently, images recorded by the slow, 30-Hz CCD camera represent the spatial distribution of mass-filtered ions recorded at a precise swat delay relative to the initial laser pulse. Figure 2.5b illustrates the overall pulse sequence applied to the flyswatter optics. Once the flight time, t_1 , corresponding to detection of ions having mass, m_1 , is known, any peak, t_2 , in the time-of-flight spectrum can be accurately assigned to an absolute mass, m_2 , by the relation:²

$$m_2 = m_1 \sqrt{\frac{t_2^2}{t_1^2}} \quad (2.1)$$

The critical parameters in operating the flyswatter are the voltage pulse polarities, and the swat and mass delays. The incident ion packet can be detected if the repeller is fired shortly after the ions exit the Menzinger lens and before they leave the detection

region. An image of the incident ion packet provides information regarding the spatial integrity of the ion beam as well as a quantitative measure of the number of incident ions. As the swat delay ($\sim 25 \text{ ns}$) is increased, the image of the incident ion packet on the phosphor screen moves closer to the surface. For significantly longer swat delays, the incident ions will impact the surface, and scattered product ions can be detected. Positive and negative scattered ions are distinguished by the polarity of the voltages applied to the repeller pulse, the flight-tube pulse, and the CEMA front plate.

The entire velocity distribution of scattered products is measured by collecting mass-filtered images at a series of different swat delays beginning with the time that scattered ions first reach the detector through the time that the slowest ions move out of the detection region. Reducing a series of ion images, recorded at various swat delays, to a single velocity distribution is described in Sect. 2.6. At periodic intervals during scattering experiments, the swat and mass delays are set to record an image of the incident ion packet. The integrated intensity of the ion packet image is directly proportional to the number of ions incident on the surface, and this quantity is used to normalize the scattered product distributions.

Geometrical constraints must be considered in the overall analysis. The solid angle of collection for the imaging detector is defined by acceptance angles of $\pm 28^\circ$ (in-plane) and $\pm 7^\circ$ (out-of-plane). This corresponds to a collection efficiency of approximately 3.6% of 2π steradians. The scattered flux of ions, f , is described by

$$f = \cos^n \theta \quad (2.2)$$

where θ defines the scattered angle from the surface normal and n quantifies the width of the distribution. The relative ion yield of a given scattered product is calculated as the number of collected product ions, $N_{scattered}$, integrated over all velocities within the

angular range of the detector, divided by the number of incident ions, $N_{incident}$.

$$\text{Relative ion yield} = \frac{N_{Scattered}}{N_{Incident}} \quad (2.3)$$

The following equation gives the calculation for the absolute ion yield, which accounts for the geometrical constraints of the detector

$$\text{Absolute ion yield} = \frac{N_{Scattered}}{N_{Incident}} \left[\frac{100}{f} \right] \quad (2.4)$$

The absolute ion yield represents the fraction of all incident ions converted to product ions.

2.5.2 Optimization

The time-of-flight (TOF) mass spectra collected in various scattering experiments revealed some unusual shapes in the distributions. Figure 2.6 illustrates this unusual behavior when the flight time of the product cations are measured for state-selected ammonia ions scattered from a D/Al(111) surface. One of the most significant challenges with the TOF mass spectra obtained in these experiments was the inability to easily distinguish the mass distribution, or mass assignment, for each scattered product. To avoid using deconvolution techniques, the scattering experiments require very high mass resolution (1 amu), which has not been achieved with the current detector settings.

In addition to the low mass resolution, some TOF mass spectra obtained with the current apparatus reveal a shoulder that appears either at slower or faster flight times compared to the peak values. For example, when Morris *et al*¹¹ scattered state-selected

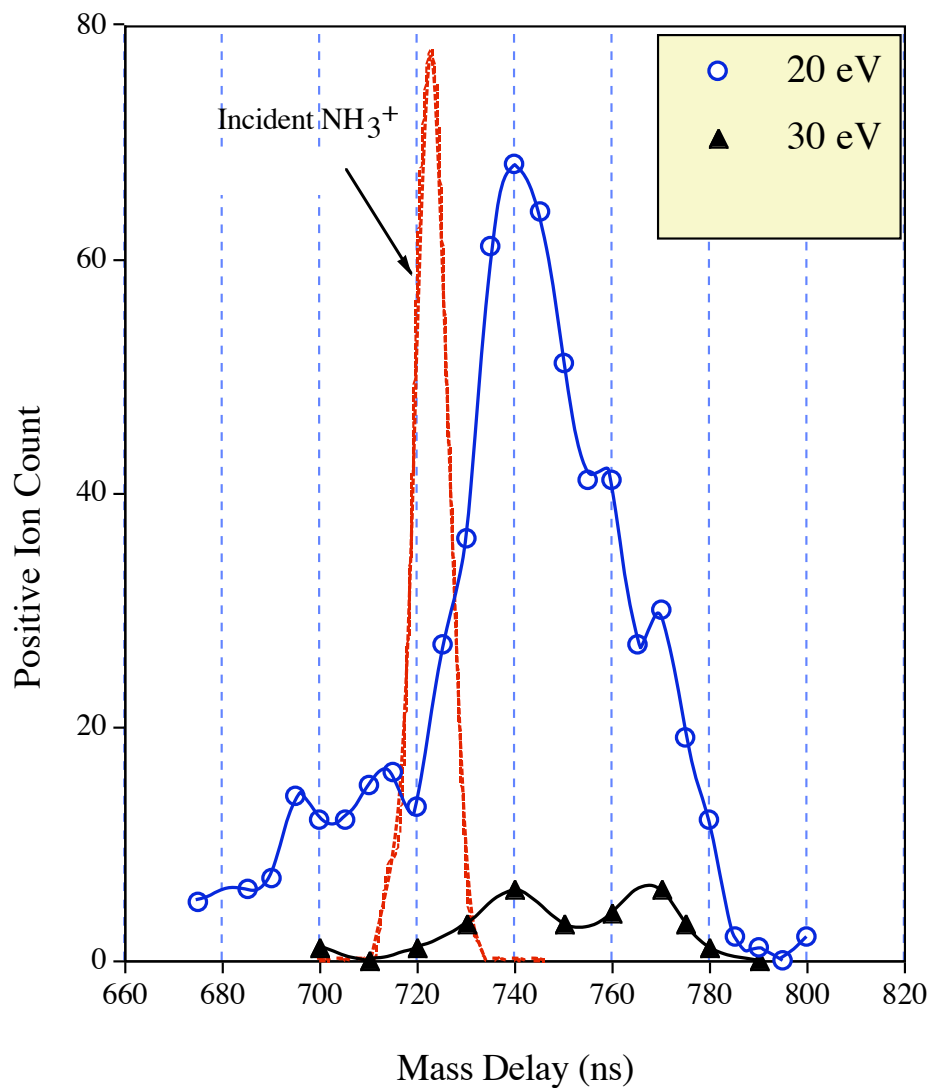


Figure 2.6 The intensity of scattered positive ions as a function of the mass delay for 20 eV and 30 eV incident NH_3^+ . The inability to easily distinguish product masses 17, 18, and 19 amu illustrates the low mass resolution of the detector for identifying the products when NH_3^+ scatters from a deuterium covered Al(111) surface. The line is drawn to guide the eye.

OCS⁺ on Ag(111), shoulders existed in the TOF distribution for each of the three detected products, O⁻, S⁻, and SO⁻ as shown in Fig. 2.7. The distribution assigned to the emergence of O⁻ has a shoulder at slower flight times compared to the 700 ns peak value, whereas a shoulder exists at faster flight times than the 1010 ns peak value for the S⁻ distribution. Investigating the mass resolution and unusual shapes of the TOF distributions through the combination of scattering experiments and Simion 3D¹² trajectory calculations reveal a TOF mass spectra sensitivity to the voltage values applied to the elements in the flyswatter. Therefore, the voltages are optimized to improve the mass resolution and to determine the factors that cause the unusual behavior observed in the TOF mass spectra.

Simion 3D¹² is a computer program designed by the Idaho National Engineering Lab to simulate the trajectory of charged particles through a set of electric and/or magnetic fields created by electrodes. The first step before running ion trajectory simulations is the creation of a Simion¹² Geometry file (Appendix A.1) to model the flyswatter, the surface, and the final deceleration lens as shown in Figure 2.8. Although Simion¹² has a very efficient method to create symmetrical ion optics, the complex repeller plate shape (Fig. 2.8 (c)) requires the creation of a geometry file. The final geometry file, NSFGEOM1.GEM includes several intricate details, including the screws, nuts, and ceramics on the repeller plate, to ensure that the simulated potential curves are close to the actual electric fields created in the experiment. Since the current apparatus contains three grids, some of the grid points are defined in the geometry file. However, the remaining grid points are defined manually, due to the limitations of the geometry files. When all the points in the electrode assembly are completely defined, the file must be compiled to calculate the electric fields in the flyswatter. The mass, charge, incident kinetic energy, and incident positions of the projectiles are defined to simulate the trajectories of scattered ions passing through the detector.

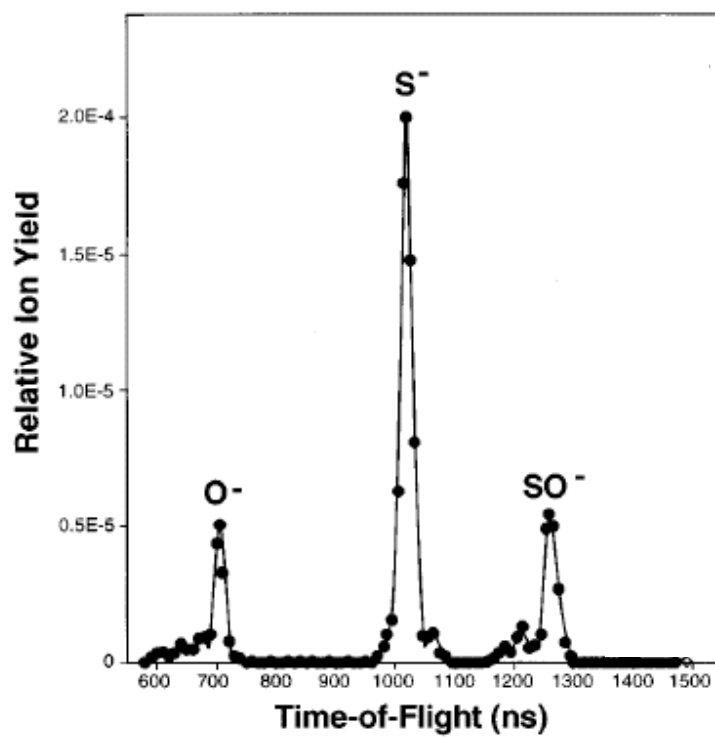


Figure 2.7 Time-of-flight mass spectrum for scattered anions produced when OCS^+ collides with $\text{Ag}(111)$ at 65 eV. (Reproduced with permission from Ref. 11).

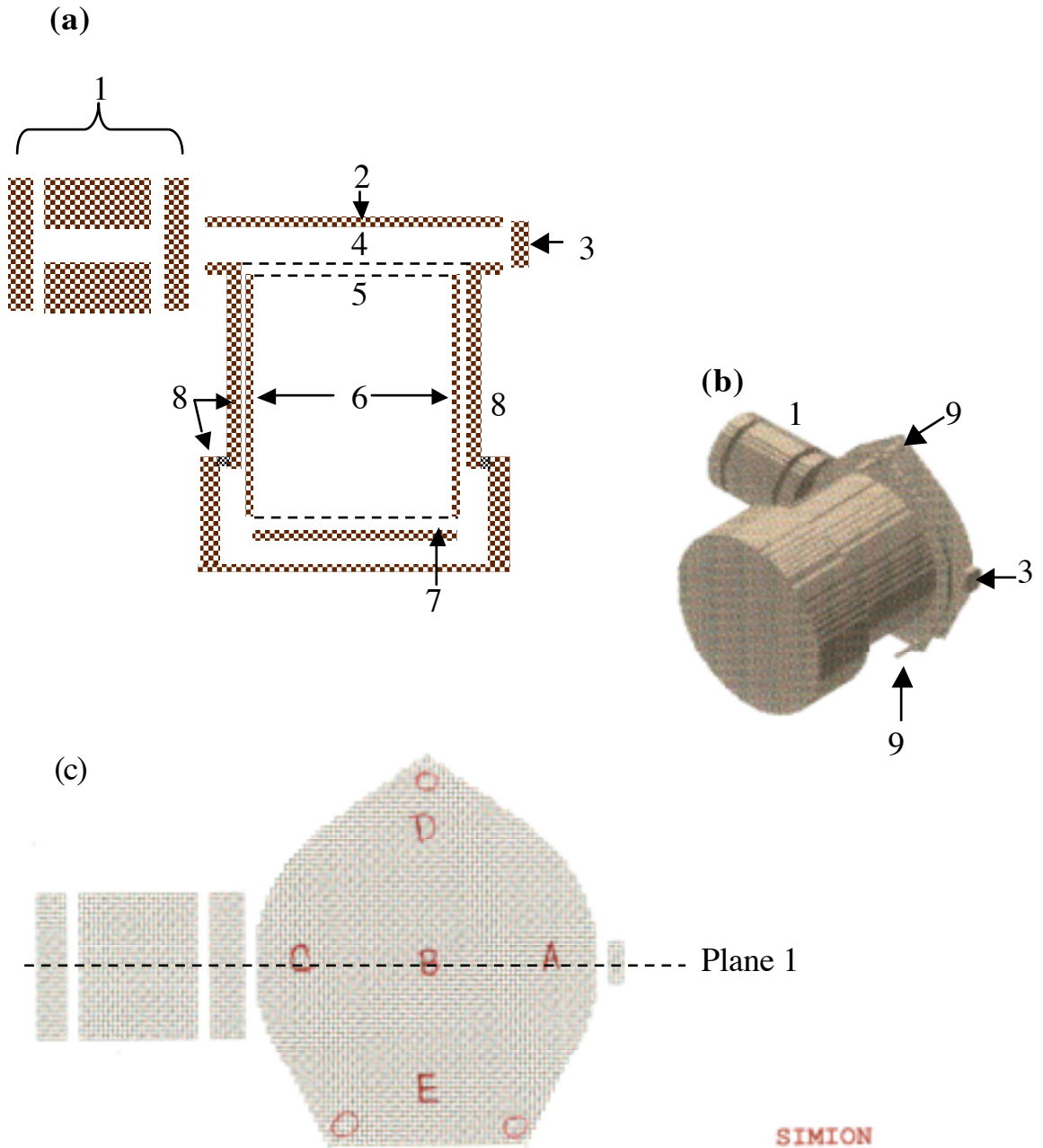


Figure 2.8 Geometry file schematics utilized for Simion 3D[®] flyswatter simulations: a) top-down view at Plane 1 b) side view of the flyswatter looking at the repeller plate with initial trajectory positions labeled A, B, C, D, and E c) an overall 3D view of the flyswatter detector. The numbers indicate the following parts: 1 Menzinger lens, 2 Repeller plate, 3 Surface, 4 Grounded grid, 5 Biased Flight Tube Grid, 6 Flight Tube, 7 CEMA Plates, 8 Grounded Tube, 9 Bolt, Nut, and Ceramic assembly.

In order to run realistic trajectories, the simulations require accurate time delays for the pulsing scheme illustrated in Fig. 2.5b. Moreover, the electronics utilized in the current apparatus include a rise time, or a ramp from 0 V to the final voltage value, which can affect the path and flight time of the ions. The rise times measured on the oscilloscope for the repeller pulse and flight tube pulse are 70 ns and 79 ns, respectively. The creation of a novel Simion TOF program (Appendix A.2) allows for the adjustment of the voltages applied to each electrode in the detector according to a specific pulse sequence with realistic pulse rise times on the repeller and flight tube elements. In order to optimize the detector, the electrode voltages, rise times, and pulse delays are systematically varied while Simion calculates the time-of-flight through the detector for ions of mass 16, 17, and 18. The time of flight is defined as the time between the rise of the swat pulse and the arrival of the ion at the CEMA plates. In addition, the initial position of each incident ion is systematically varied between the repeller and the grounded grid. The scattering angle of each ion leaving the surface is also systematically varied to simulate the scattered distribution of product ions. The flight time, final kinetic energy, and final position for each ion in the simulation is recorded and saved into a delimited text file for further analysis.

The initial simulations investigated the effects of the Menzinger lens, and the bolt assembly (screw, nut, and ceramics) on the scattered ion trajectories. The time of flight was calculated for mass 17 (NH_3) positive ions with 3 eV of kinetic energy. For each initial position A, B, C, D, and E (see Fig. 2.8 c) the flight times for 150 ions were recorded and represented in a histogram as shown in Fig. 2.9. Each value represented along the x -axis represents a 10 ns bin of flight times (i.e. 620 ns corresponds to the bin 620 ns – 630 ns). These results suggest that the perturbation to the electric field by the Menzinger lens and screw assembly does not significantly alter the TOF of the scattered ions.

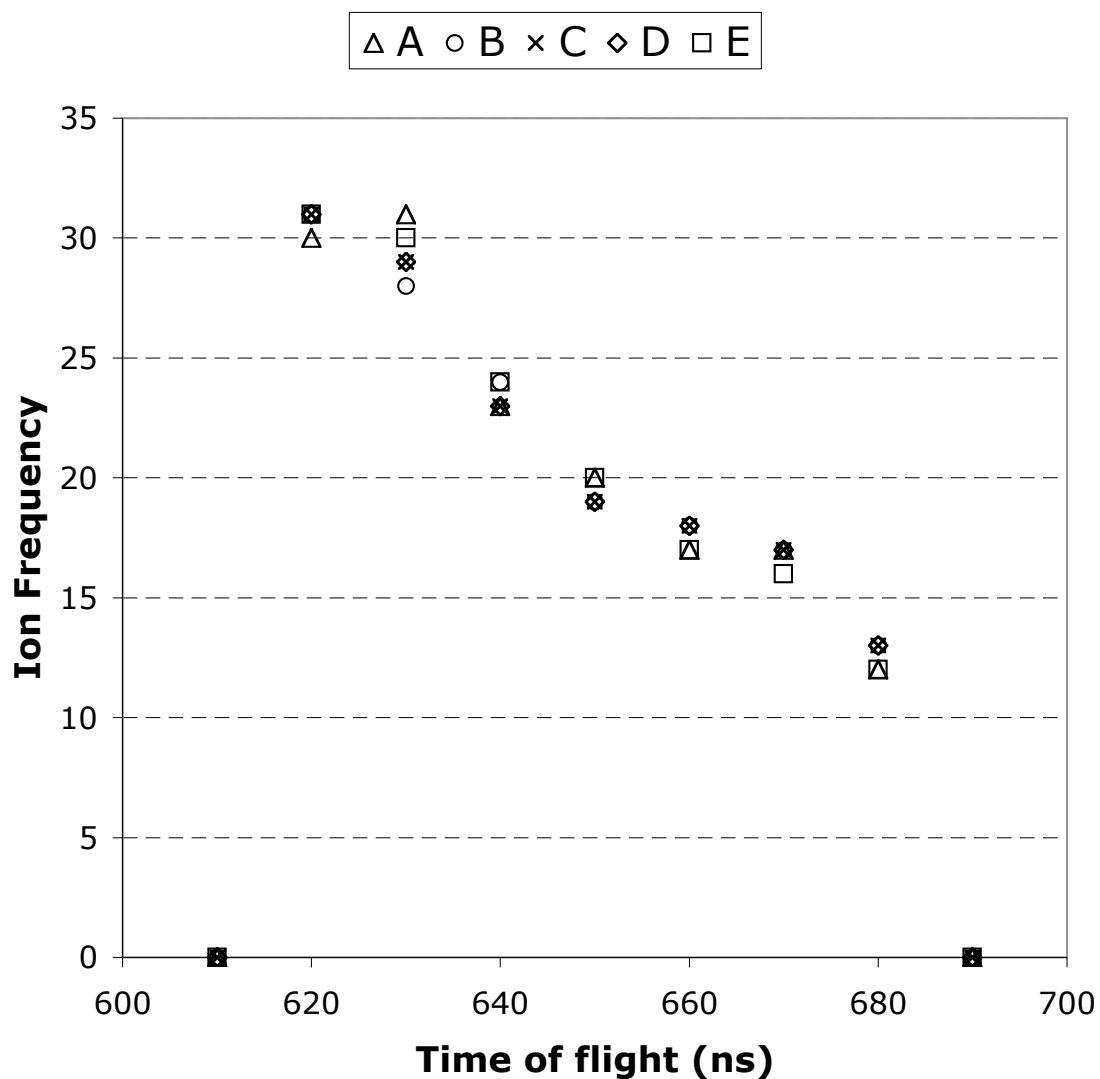


Figure 2.9 A histogram representing the flight times of 3 eV NH_3^+ originating at positions A, B, C, D, and E (see Fig. 2.8 c). For each position, the initial location of 150 ions was varied systematically between the repeller plate and the grounded grid. Each number along the x -axis corresponds to a 10 ns wide bin. The simulated electrode voltages were Repeller Plate = +970 V, Flight Tube = -840 V, CEMA = -1200 V, and Menzinger Lens = -160 V.

Surprisingly, the histogram also reveals a TOF width greater than 60 ns for a 17 amu particle for the selected set of electrode voltages. This broad width compromises the mass resolution of the flyswatter. Figure 2.10 represents the predicted TOF distribution when an equal number of ions with mass 17, 18, and 19 amu is simulated. Although the fastest particles reach the CEMA plates 665 ns after the pulse on the repeller and the slowest particles reach the detector as late as 900 ns after the repeller pulse, the majority of the ions reach the CEMA within 100 ns of the fastest particles. The most distressing part of the histogram is the overlap of the three masses at several ion flight times, consistent with poor TOF mass resolution. The electrode voltages and mass delay values utilized in the simulations correspond to the experimental conditions that resulted in the low mass resolution for scattered NH_3^+ (17 amu), NH_2D^+ (18 amu), and NHD_2^+ (19 amu).

Since the simulations accurately reproduced the conditions leading to low mass-resolution, can the simulations be used to optimize the resolution of the flyswatter? One proposal to improve the resolution involves decreasing the rise time of the pulsed electronics. However, a series of simulations revealed that the overall flight time is not significantly affected by the rise time values. Instead, the ratio of the repeller plate voltage (RV) to the flight tube voltage (FTV) significantly affects the flight times and the trajectories of the ions.

The sensitivity of the scattered product TOF distribution to the electrode voltages is investigated through a series of trajectories calculated for 17-, 18-, and 19-amu positive ions initiated at various positions between the repeller plate and the grounded grid. Figure 2.11 represents the flight times for each mass as a function of the initial z position (location between the repeller plate and grounded grid) for the corresponding RV and FTV values (a) RV = +970 V, FTV = -840 V, (b) RV = +670 V, FTV = -840 V, and (c) RV = +970 V, FTV = -1080 V. The voltages on the Menzinger lens and CEMA

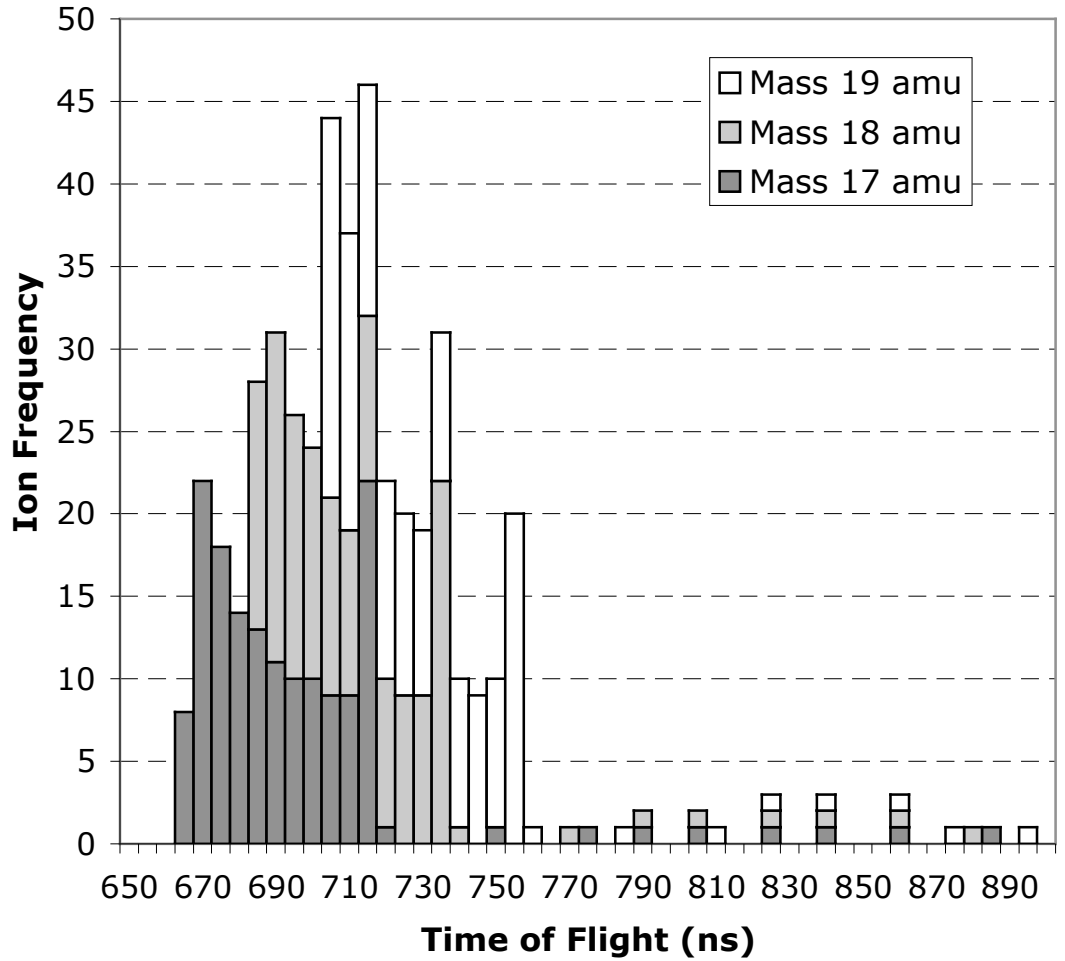


Figure 2.10 A histogram with a 5 ns bin width representing the flight times of 3 eV positive ions with 17, 18, and 19 amu originating at position B (see Fig. 2.8 c). The initial location of 150 ions for each mass varied systematically between the repeller plate and the grounded grid. The simulated electrode voltages were Repeller Plate = +970 V, Flight Tube = -840 V, CEMA = -1200 V, and Menzinger Lens = -160 V.

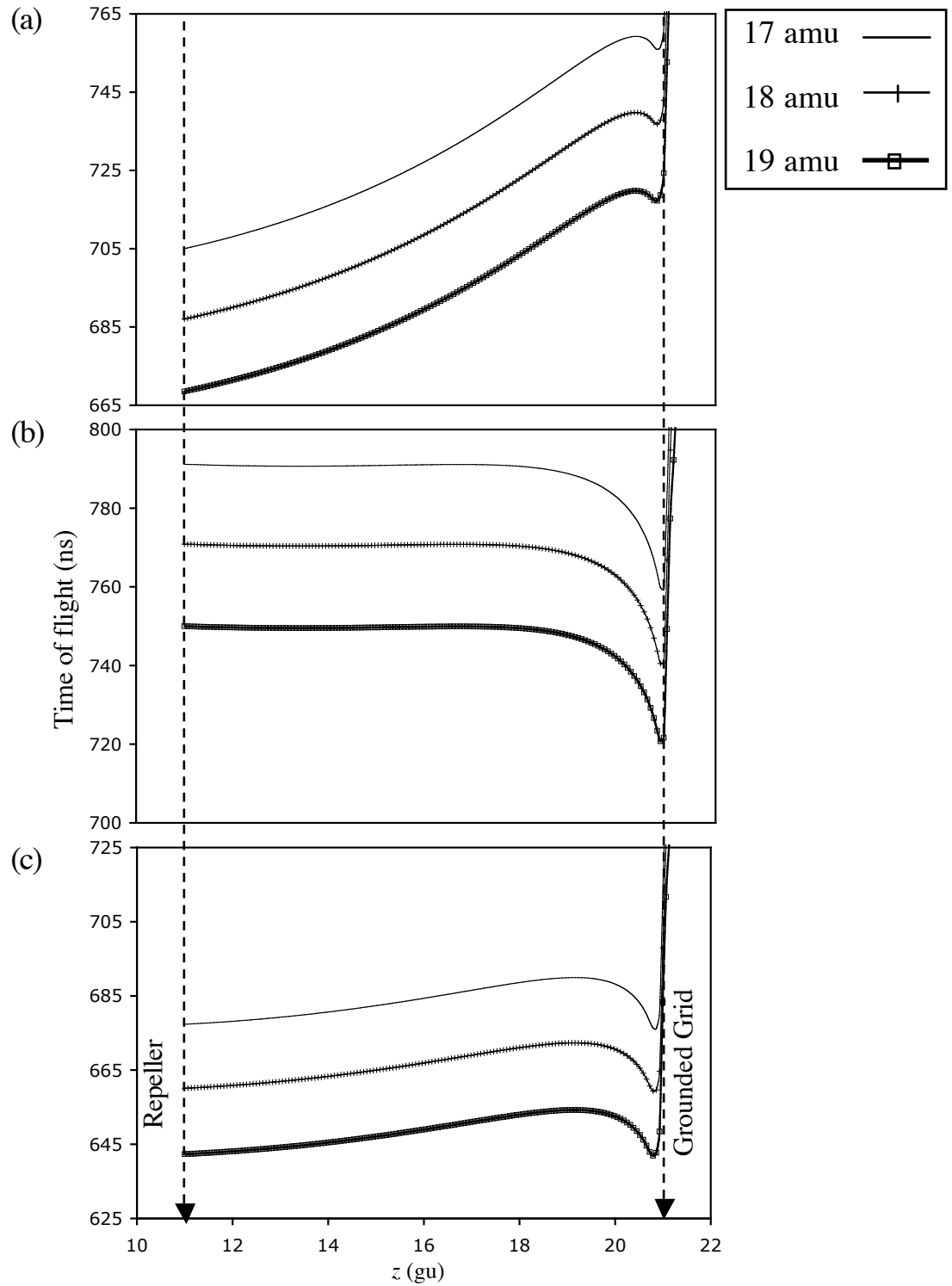


Figure 2.11 Simion trajectory calculations for positive ions traveling from the region between the repeller plate ($z = 11$) and the grounded grid ($z=21$) to the CEMA plates for various repeller plate (RV) and flight tube (FTV) electrode potential values (a)[RV = +970 V, FTV = -840 V] (b)[RV = +670 V, FTV = -840 V], and (c)[RV = +970 V, FTV = -1080 V], respectively. The TOF for 17, 18, and 19 amu ions is calculated as a function of the initial position of the ion.

plates are held constant at +160 V and -1200 V, respectively, consistent with the experimental values. When comparing a particular mass, the difference in the shapes of the curves is quite significant, where graph (a) results in the broadest distribution of TOF values. The product ions that scatter closest to the repeller plate result in the shortest flight times to the CEMA plates, whereas the voltage conditions for (b) result in a relatively constant TOF value, except for the ions located closest to the grounded grid at the time of the repeller pulse. The corresponding flight time widths for (a), (b), and (c) are approximately 60 ns, 25 ns, and 20 ns, respectively. Due to the large distribution of flight times, the electrode voltage combination for (a) results in the worst conditions for resolving product masses.

The prediction for the mass resolution for the voltage conditions used in Fig. 2.11 (b) and (c) is more difficult than in (a). Moreover, the ion packets utilized in the scattering experiments can be approximated to have a Gaussian distribution, where the greatest intensity of ions is located at the center between the repeller plate and grounded grid. Therefore, the weighted TOF distribution of 176 cations each of mass 17, 18, and 19 amu is calculated for each electrode voltage combination. The results shown in Fig. 2.12 show a significant dependence of the TOF distribution to the repeller and flight tube voltages. The highest mass resolution occurs for the flyswatter voltages utilized in (b) $RV = +670$ V and $FTV = -840$ V. However, these voltage conditions also produce shoulders at lower mass delay values compared to the peak values. These shoulders are due to the ions that scatter within 2 grid units ($2.5 \text{ gu} = 0.10 \text{ inches}$) of the grounded grid. Figure 2.12 (c) reveals TOF spectra with double peaks that correspond to a majority of ions reaching the CEMA plates with similar flight times. However, the scattered ions that are between 1 and 3 gu away from the grounded grid at the time of the pulse on the repeller plate result in slower flight times compared to ions originating at other initial positions between the repeller and grounded grid. When comparing

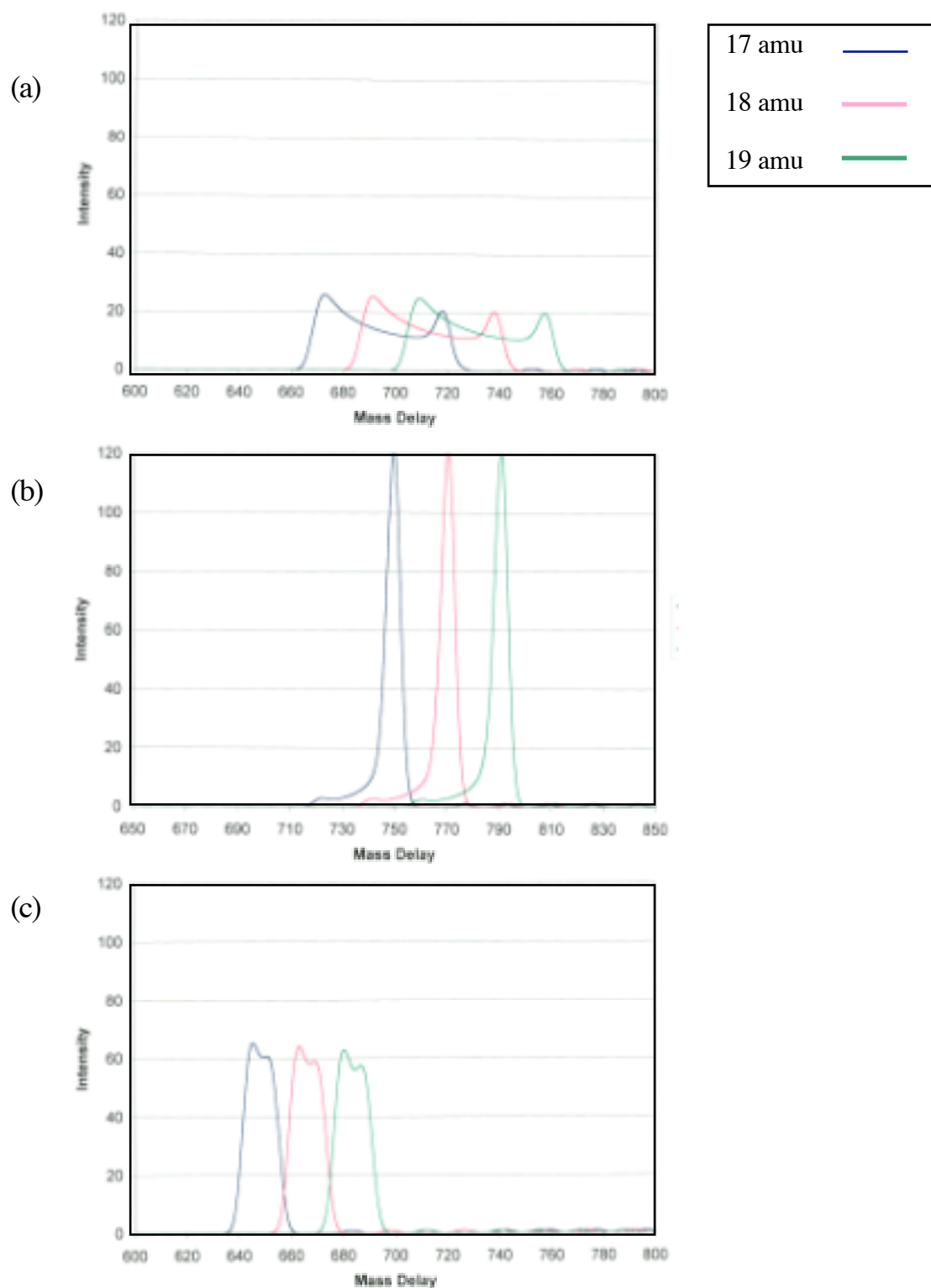


Figure 2.12. Simion[®] trajectory mass delay calculations for the intensity of positive ions of mass 17, 18, and 19 amu for various repeller plate (RV) and flight tube (FTV) electrode potential values (a)[RV = +970 V, FTV = -840 V] (b)[RV = +670 V, FTV = -840 V], and (c)[RV = +970 V, FTV = -1080 V], respectively.

Fig. 2.12 (a), (b), and (c), the electrode voltages utilized for (b) result in the best mass resolution in the TOF spectrum.

In order to confirm the results of the Simion 3D⁺ simulations, the best combination of electrode potentials are utilized in the experiment for scattering state-selected NH_3^+ on a D/Pt(111) surface. Figure 2.13 illustrates the much-improved mass resolution of the detector for the ammonia scattering system. Clearly, the TOF mass spectrum resolves three products of mass 17, 18 and 19 amu at corresponding peak mass delay values at 845 ns, 870 ns, and 895 ns, respectively. Not only are the three products clearly resolved, but the distributions are also void of any shoulders at high and low mass delays compared to the peak values.

Overall, the performance of the flyswatter relies on several critical parameters. The combination of ion trajectory calculations in conjunction with scattering experiments reveals a TOF mass distribution sensitivity to the applied electrode voltages on the elements within the flyswatter. More specifically, the ratio of repeller plate voltage to flight tube voltage used in the experiments is critical for removing shoulders in the scattered product mass distributions and for resolving products with a 1 amu difference in mass.

2.6 Velocity Analysis

To compile a complete velocity distribution of a scattered product, ion images must be gathered for a series of different swat delays. This is because scattered ions routinely have broad velocity distributions that extend beyond the dimensions of the image detector for any single swat delay. Real-time processing of the images results in a list of (x, y) coordinates for each detected ion. The list of ion events is transformed into a velocity distribution by a separate velocity analysis program. Characterization of

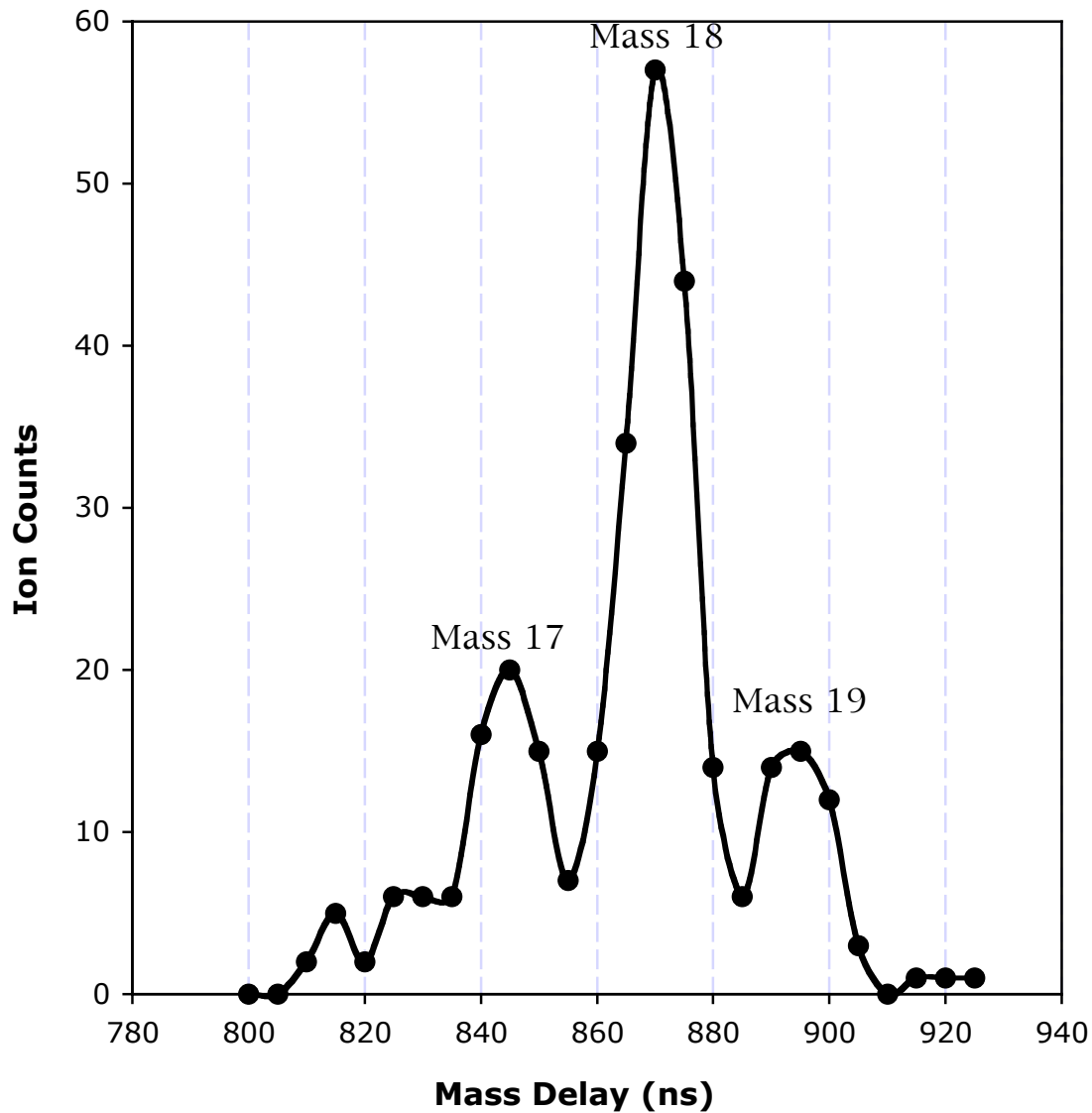


Figure 2.13 Time of flight mass spectra for the emergence of cations when 60 eV NH_3^+ is scattered on D/Pt(111). The voltages applied to the repeller plate and flight tube are +650 V and -805 V, respectively.

the incident ion packet allows one to determine the (x, y) position and the time at which the incident ion packet strikes the surface. Relative to this reference point, the velocity of all scattered ions can be determined from the distance traveled between the point of surface impact and the scattered ion position, divided by the time lapsed between surface impact and scattered-ion collection (swat delay + mass delay). Appropriate weightings for each ion are calculated from geometrical considerations.⁶ A 2-D velocity distribution is generated by sorting the recorded ion events into a 2-D velocity grid and assigning the relative intensity in each grid element to the sum of the relevant ion weightings. This can be collapsed to a 1-D velocity distribution by integrating the 2-D velocity distribution over all final scattering angles.

The shape of the final 1-D velocity distribution is fairly sensitive to the chosen series of swat delays. Figure 2.14 illustrates the various shapes of the velocity distribution for different sets of swat delays when 44 eV Br_2^+ ions scatter from a Pt(111) surface resulting in the emergence of Br^- products. The velocity distribution for Set 1, corresponding to data collected for the combination of 48, 52, 56, and 60 μs swat delays, has a peak near 2500 m/s. This peak shifts to ~ 1900 m/s with a greater intensity for the 50, 54, 58, and 62 μs swat delays utilized in Set 2. When the data from Sets 1 and 2 are analyzed together, the shape of the resulting velocity distribution is a combination of the two sets—a peak near 1900 m/s and a shoulder near 2500 m/s. Although the deviations in the relative peak intensities and positions do not significantly affect the mean velocity value of the emerging ions, obtaining accurate shapes for the velocity distributions is crucial for curve fitting routines, similar to the ones described in Chapter 3. Therefore, for each bromine final beam energy a series of ten swat delays is utilized to create the most accurate final 1-D velocity distributions (Chapters 3 and 4).

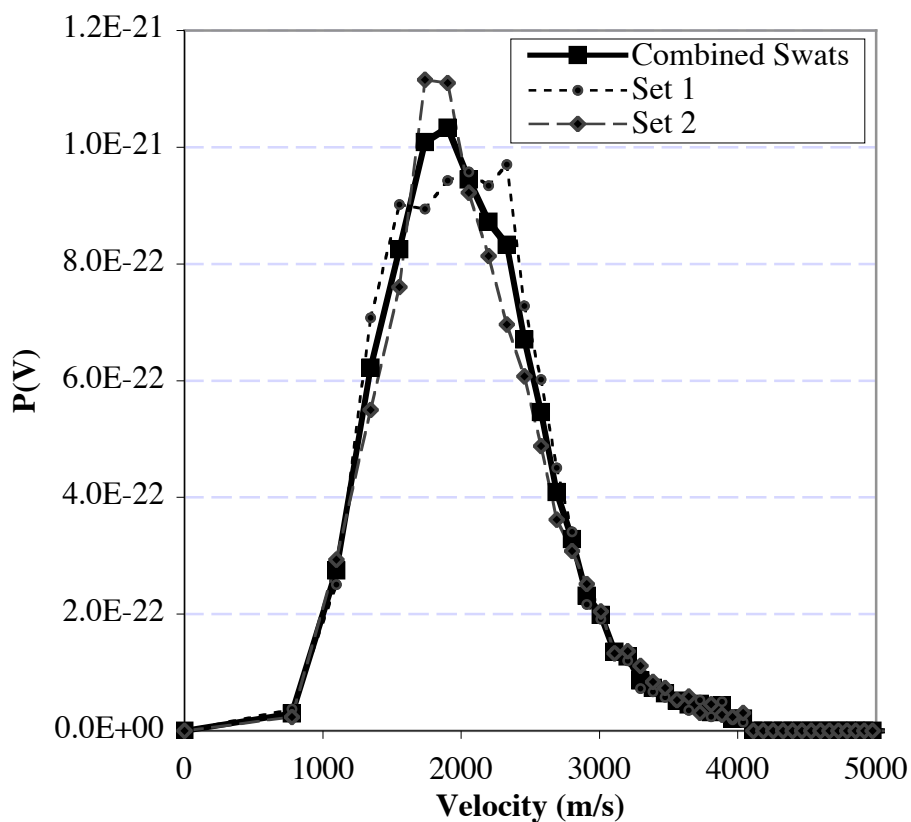


Figure 2.14 A comparison of scattered Br^- velocity distributions for various combinations of swat delays. The distribution for Set 1 corresponds to data collected for the combination of 48, 52, 56, and 60 μs swat delays. The data for Set 2 correspond to data collected for swat delays equal to 50, 54, 58, and 62 μs . The velocity distribution for the combined swats is the result of analyzing the data from the eight swat delays together.

In conclusion, a complex experimental apparatus is utilized to investigate the operative fundamental mechanisms when state-selected incident ions scatter from well-characterized surfaces. After the preparation of the surface and formation of positive incident ions, the voltages on the ion imaging detector are carefully chosen to optimize the mass resolution and shapes of the TOF mass distributions. The images of scattered product ions captured by the detector are saved for further analysis to calculate the product yields, average kinetic energies, velocity distributions, and scattered angles. A detailed analysis of each of these data sets allows one to describe the reaction dynamics for reactive scattering experiments.

2.7. References

- ¹ J. S. Martin, J. N. Greeley, J. R. Morris, and D. C. Jacobs, *Journal of Chemical Physics* **97** (12), 9476 (1992).
- ² J. S. Martin, J. N. Greeley, J. R. Morris, B. T. Feranchak, and D. C. Jacobs, *Journal of Chemical Physics* **100** (9), 6791 (1994).
- ³ J. R. Morris, Doctoral, University of Notre Dame, 1996.
- ⁴ M. Maazouz, J. R. Morris, and D. C. Jacobs, *Ion Imaging in Surface Scattering*. (American Chemical Society, Washington, D.C., 2001).
- ⁵ J. N. Greeley, Doctoral Thesis, University of Notre Dame, 1995.
- ⁶ D. Corr and D. C. Jacobs, *Review of Scientific Instruments* **63** (3), 1969 (1992).
- ⁷ S. L. Anderson, *Advances in Chemical Physics* **82**, 177 (1992).
- ⁸ B. G. Koenders, G. J. Kuik, K. E. Drabe, and C. A. De Lange, *Chemical Physics Letters* **147** (4), 310 (1988).
- ⁹ M. C. Wiley and I. H. McLaren, *Review of Scientific Instruments* **26**, 1150 (1955).
- ¹⁰ F. Chandezon, B. Huber, and C. Ristori, *Review of Scientific Instruments* **65** (11), 3344 (1994).
- ¹¹ J. R. Morris, G. Kim, T. L. O. Barstis, R. Mitra, and D. C. Jacobs, *Journal of Chemical Physics* **107** (16), 6448 (1997).
- ¹² D. A. Dahl, Simion 3D (Idaho National Engineering Laboratory, Idaho Falls, ID, 1995).